

Tuning ultrafast electron thermalization pathways in a van der Waals heterostructure

Qiong Ma^{1†}, Trond I. Andersen^{1†}, Nityan L. Nair^{1†}, Nathaniel M. Gabor^{1*}, Mathieu Massicotte², Chun Hung Lui¹, Andrea F. Young¹, Wenjing Fang³, Kenji Watanabe⁴, Takashi Taniguchi⁴, Jing Kong³, Nuh Gedik¹, Frank H. L. Koppens^{2,5} and Pablo Jarillo-Herrero^{1*}

Ultrafast electron thermalization—the process leading to carrier multiplication via impact ionization^{1,2}, and hot-carrier luminescence^{3,4}—occurs when optically excited electrons in a material undergo rapid electron–electron scattering^{3,5–7} to redistribute excess energy and reach electronic thermal equilibrium. Owing to extremely short time and length scales, the measurement and manipulation of electron thermalization in nanoscale devices remains challenging even with the most advanced ultrafast laser techniques^{8–14}. Here, we overcome this challenge by leveraging the atomic thinness of two-dimensional van der Waals (vdW) materials to introduce a highly tunable electron transfer pathway that directly competes with electron thermalization. We realize this scheme in a graphene–boron nitride–graphene (G–BN–G) vdW heterostructure^{15–17}, through which optically excited carriers are transported from one graphene layer to the other. By applying an interlayer bias voltage or varying the excitation photon energy, interlayer carrier transport can be controlled to occur faster or slower than the intralayer scattering events, thus effectively tuning the electron thermalization pathways in graphene. Our findings, which demonstrate a means to probe and directly modulate electron energy transport in nanoscale materials, represent a step towards designing and implementing optoelectronic and energy-harvesting devices with tailored microscopic properties.

Immediately after photoexcitation of an optoelectronic device, energetic electrons scatter with other high-energy and ambient charge carriers to form a thermalized hot electron gas, which further cools by dissipating excess energy to the lattice. Owing to the short distance travelled by charge carriers between electron–electron scattering events in solids¹⁸, equilibration among the electrons occurs on timescales from tens of femtoseconds to picoseconds^{19,20}. In graphene, a low-dimensional material with much enhanced Coulomb interaction²¹, electron thermalization is known to occur on extremely fast timescales (<30 fs; refs 22–25), reflecting the extremely short transit length between scattering events. Most analyses of graphene have, therefore, treated its electrons as being instantaneously thermalized^{26–29}, and slightly non-thermal electronic behaviour has thus far only been reported in pump-probe experiments with ultrashort (~10 fs) laser pulses and low excitation density^{8,9}. Owing to such short time (femtosecond) and length (nanometre) scales, it is challenging to detect and control

the thermalization process in graphene or, more generally, in any solid-state systems.

In this letter, we report an approach to probe and manipulate the electron thermalization in graphene by introducing a new energy transport channel that competes with the thermalization process. Such an additional dynamical pathway is realized in a vdW heterostructure³⁰ that consists of a G–BN–G stack (Fig. 1a–c). In this layered structure, the photoexcited electrons in one graphene layer can travel vertically to the other graphene layer through the very thin middle BN layer (blue dashed arrow in Fig. 1b). Given the close proximity of these layers, interlayer charge transport can occur on extremely fast timescales³¹, and thus compete directly with the intralayer thermalization process (red arrows in Fig. 1b). In our experiment, we have observed such competing processes by measuring the interlayer photocurrent under different bias and excitation conditions. Remarkably, by adjusting the interlayer bias voltage or varying the excitation photon energy, we can control the interlayer charge transport to occur slower or faster than the intralayer thermalization, thus tuning the thermalization process. Our experiments not only provide valuable insight into the electron dynamics of graphene, but also demonstrate a means to manipulate electron thermalization in low-dimensional materials.

We fabricated the G–BN–G heterostructure devices on Si/SiO₂ substrates by mechanically co-laminating graphene sheets and hexagonal boron nitride (BN) flakes³² with 5–30 nm thickness (Fig. 1a,d; see Methods). In our experiment, we applied a bias voltage V_b between the top and bottom graphene and measured the corresponding interlayer current I under optical excitation. The main light source is a broadband supercontinuum laser that provides bright semi-continuous radiation from wavelength $\lambda = 450$ to 2,000 nm (see Methods). To probe the interlayer current in the time domain, we also used femtosecond laser pulses from an 80 MHz Ti:sapphire oscillator. We have measured four G–BN–G devices with monolayer graphene and two devices with few-layer (\leq four layers) graphene, and found similar results. The device characteristics are therefore insensitive to a slight change of graphene layer thickness.

Figure 1d–f shows the optical image of a G–BN–G device and the corresponding device characterization using scanning photocurrent microscopy. Photocurrent images at interlayer bias voltages $V_b = -0.5$ and 0.5 V under laser excitation at a wavelength of 600 nm show that the photocurrent I appears only in the

¹Department of Physics, Massachusetts Institute of Technology, Cambridge, Massachusetts 02139, USA. ²ICFO-Institut de Ciències Fotoniques, The Barcelona Institute of Science and Technology, 08860 Castelldefels (Barcelona), Spain. ³Department of Electrical Engineering and Computer Science, Massachusetts Institute of Technology, Cambridge, Massachusetts 02139, USA. ⁴National Institute for Materials Science, Namiki 1-1, Tsukuba, Ibaraki 305-0044, Japan. ⁵ICREA - Institució Catalana de Recerca i Estudis Avançats, 08010 Barcelona, Spain. [†]These authors contributed equally to this work. *e-mail: nathaniel.gabor@ucr.edu; pjarillo@mit.edu

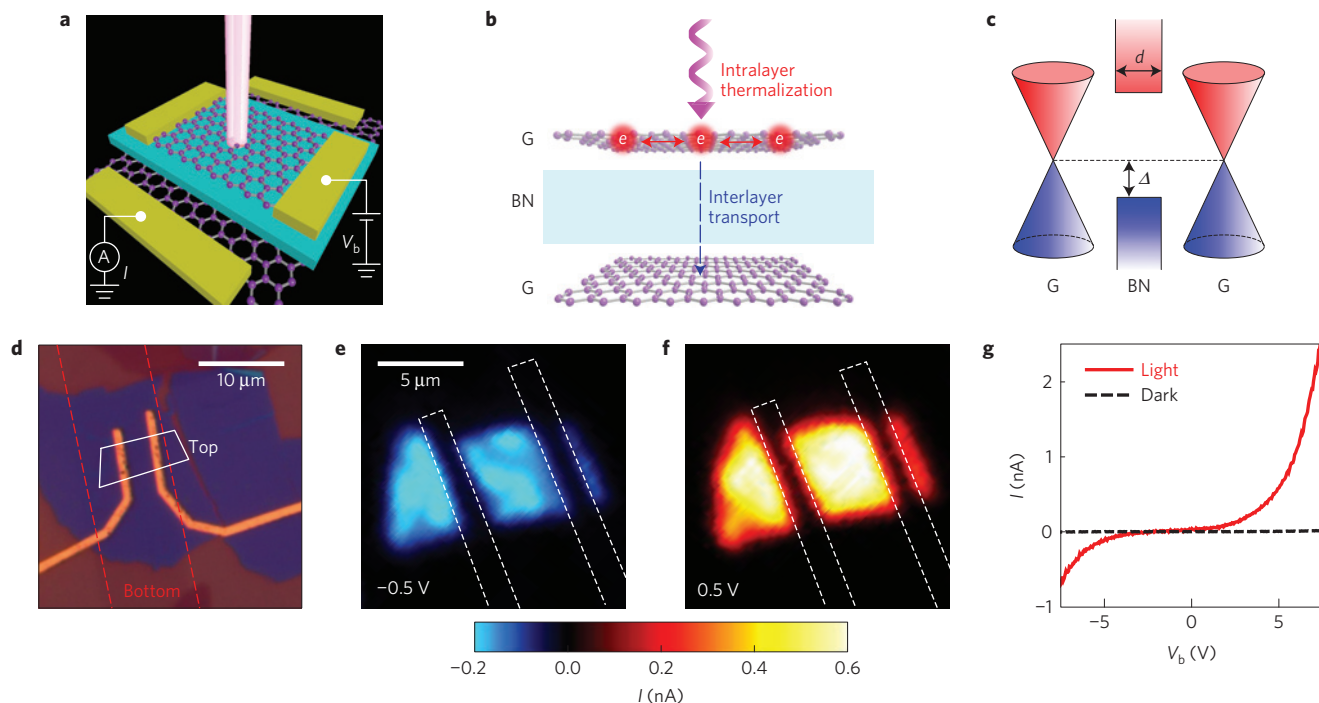


Figure 1 | Interlayer photocurrent of a G-BN-G device. **a**, Schematic of a G-BN-G device under optical excitation. **b**, Schematic of intralayer thermalization and interlayer transport of the optically excited carriers. **c**, Band alignment between graphene and BN. BN has a band gap of ~ 5.9 eV, and the Dirac point of graphene is located ~ 1.3 eV (Δ) above the edge of the BN valence band³³. **d**, Optical image of a G-BN-G device, which consists of a top exfoliated graphene layer (white line), a 14-nm-thick BN flake, and a bottom graphene layer grown by chemical vapour deposition (dashed red line). **e, f**, Scanning images of interlayer photocurrent at interlayer bias $V_b = -0.5$ and 0.5 V, respectively. **g**, Interlayer photocurrent as a function of V_b with and without light illumination. All measurements were carried out with 600-nm optical excitation from a supercontinuum laser at $T = 100$ K. The incident laser power is 500 μW for **e, f** and 100 μW for **g**.

area where the two graphene layers overlap with each other. The photocurrent magnitude increases significantly with V_b , and its direction flips with the sign of bias voltage (Fig. 1g). We do not observe any current in the absence of illumination, indicating that optical excitation is necessary to generate a measurable interlayer current in our G-BN-G devices. On the basis of recent first-principles calculations³³, the graphene Dirac point is located at $\Delta \sim 1.3$ eV above the BN valence band edge, and ~ 4.5 eV below the conduction band edge (shown schematically in Fig. 1c), in agreement with dark tunnelling measurements^{15,16}. This suggests that, because the potential energy barrier Δ is much smaller for positive charge carriers (holes) than for electrons, the interlayer current is mediated predominantly by holes.

The photocurrent in our G-BN-G devices exhibits a complex dependence on excitation laser power P , interlayer bias V_b , and excitation photon energy $\hbar\omega$ (Fig. 2). Although the photocurrent generally increases with laser power, it exhibits both linear and superlinear power dependences, depending sensitively on bias voltage and photon energy. If we keep a constant bias $V_b = 5$ V, I increases superlinearly with P at $\hbar\omega = 1.75$ eV (red dots in the left panel of Fig. 2a), yet gradually becomes linear as the photon energy increases to $\hbar\omega = 2.43$ eV (purple squares). If we instead keep a constant photon energy $\hbar\omega = 2.10$ eV, the photocurrent increases superlinearly with P at $V_b = 1.5$ V (red dots in the right panel of Fig. 2a), then gradually becomes linear as the bias increases to $V_b = 10$ V (purple squares).

Remarkably, the complexity of the photocurrent variations can be efficiently captured by a single fitting parameter γ , which we obtained by fitting all photocurrent versus power data with a simple power law $I \sim P^\gamma$. Figure 2b, our main result, shows γ over a wide range of bias voltage and photon energy. The data is separated into several distinct regions, labelled A and B, highlighting the

superlinear ($\gamma > 1$, red–yellow colour) and linear ($\gamma = 1 \pm 0.02$, blue) power dependence of the photocurrent, respectively. The value of γ demonstrates a clear and gradual transition from $\gamma \sim 3$ at low bias and photon energy (regime A) to $\gamma \sim 1$ at high bias voltage and photon energy (regime B; see Supplementary Information).

We attribute the complex photocurrent behaviour to the transition between two distinct processes, thermionic emission and direct carrier tunnelling, both of which mediate charge carrier transit through the G-BN-G heterostructure (Fig. 2c). In thermionic emission, the photoexcited carriers remain in the graphene, scatter with one another, and quickly reach thermal equilibrium among themselves. High-energy carriers in the hot tail of the resultant thermal distribution have sufficient energy to overcome the potential energy barrier Δ , and will travel to the other graphene layer^{34–36}. Whereas previous studies^{29,37} have shown that the temperature of hot carriers in graphene scales with laser power approximately as $T \sim P^{1/3}$, the population of thermionically emitted carriers increases exponentially with the temperature for the high BN barrier. We therefore expect an overall superlinear dependence of the photocurrent on the laser power³⁴ (see Supplementary Information). This behaviour matches well with our observation at low $V_b/\hbar\omega$ (Regime A in Fig. 2b,c).

In contrast, at high $V_b/\hbar\omega$, the effective BN barrier is reduced, allowing the excited carriers to tunnel from one graphene layer to the other before they scatter with other carriers. Given the energy height and thickness of the BN potential energy barrier, optical excitation is necessary to assist the tunnelling process^{15,16}. The photon-assisted tunnelling current then scales with the number of initial photoexcited carriers and, therefore, increases linearly with laser power. This behaviour matches well with the observed linear power dependence of photocurrent at high $V_b/\hbar\omega$ (Regime B in Fig. 2b,c).

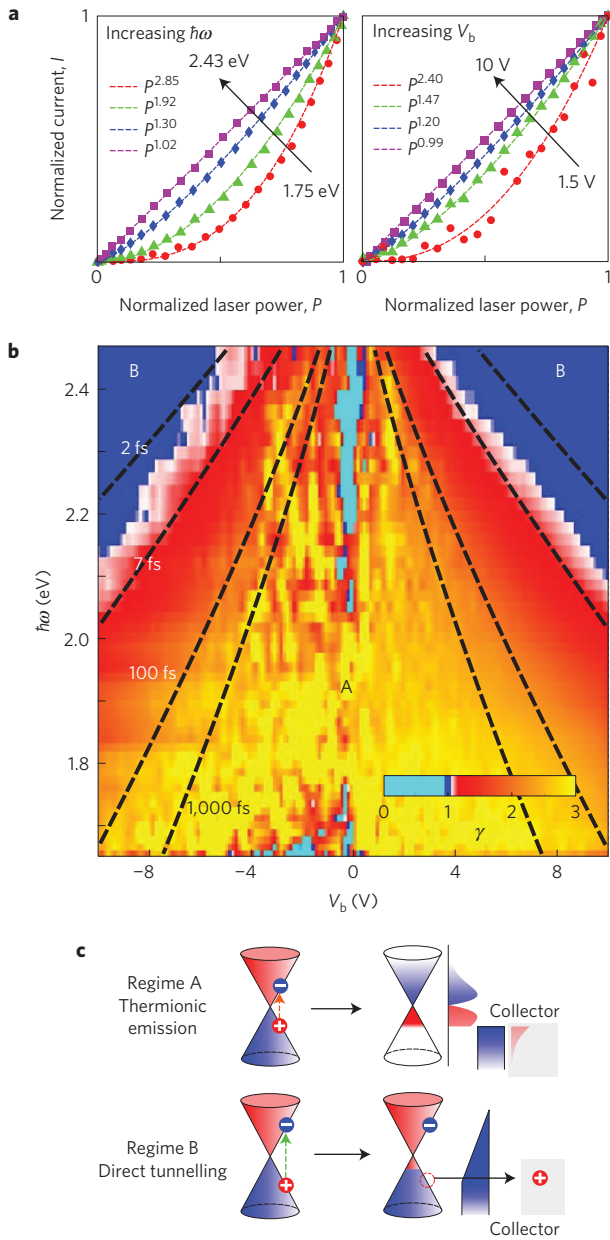


Figure 2 | Two different regimes of interlayer photocurrent in a G-BN-G device. **a**, Photocurrent I as a function of excitation laser power P , at constant interlayer bias $V_b = 5$ V but increasing photon energies $\hbar\omega = 1.75, 2.10, 2.25$ and 2.43 eV (left panel), and at constant photon energy $\hbar\omega = 2.10$ eV but increasing bias $V_b = 1.5, 3.75, 5$ and 10 V (right panel). For better comparison, the current and laser power are normalized, and the data are fitted with a power law $I \sim P^\gamma$. The raw data are shown in the Supplementary Information. **b**, Colour map of γ as a function of V_b and $\hbar\omega$. The colour scale is customized to make the area with $\gamma > 1$ (Region A) and $\gamma = 1 \pm 0.02$ (Region B) appear red-yellow and blue, respectively. The black dashed lines are contours corresponding to tunnelling times of 2, 7, 100 and 1,000 fs, predicted by our model described in the text. **c**, Schematics depicting the thermionic emission and the direct carrier tunnelling as the dominant photocurrent mechanism, respectively, for Region A and B in **b**. All measurements were carried out with a supercontinuum laser at $T = 100$ K.

To confirm that electron thermalization dominates the photocurrent response in the thermionic regime, we performed photocurrent measurements using a Ti:sapphire femtosecond laser at low $V_b/\hbar\omega$. At a photon energy of 1.55 eV, photoexcitation

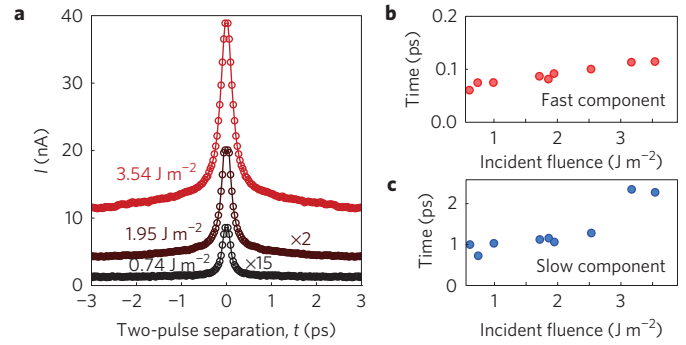


Figure 3 | Two-pulse correlation of interlayer photocurrent in a G-BN-G device. **a**, Photocurrent at $V_b = 0.1$ V, as a function of temporal separation between two identical but cross-polarized excitation pulses. The incident fluences of each beam are $0.74, 1.95$ and 3.54 J cm $^{-2}$. The pulse duration is 90 fs and the photon energy is 1.55 eV. **b, c**, The time constants of the fast and slow components, respectively, at different incident fluences. They are extracted by fitting the correlation data with a symmetric biexponential function convolved with a Gaussian function of width 130 fs. All measurements were carried out with a Ti:sapphire laser at $T = 300$ K.

with short pulses (90-fs duration) produces a photocurrent that is orders of magnitude higher than that with a supercontinuum laser (pulse duration ~ 90 ps) at the same fluence, indicating that shorter pulses produce a higher transient electronic temperature. In addition, we measured the photocurrent under photoexcitation by two identical laser pulses with orthogonal polarization (Methods) and varying temporal separation^{29,37}. We observed strong positive two-pulse correlation in the photocurrent signal, which exhibits a short component (< 100 fs) and a long component (~ 1 ps; Fig. 3 and Methods). These results, consistent with thermionic emission, are similar to the previously reported two-pulse correlation of hot photoluminescence³, a phenomenon that arises from hot carriers at the high-energy tail of the thermal distribution in graphene. Moreover, positive correlation in the two-pulse photocurrent measurement immediately excludes direct carrier tunnelling with a linear P -dependence as the main photocurrent mechanism at low V_b . We thus conclude that the observed photocurrent at low $V_b/\hbar\omega$ arises from high-energy thermalized carriers in graphene.

In the photon-assisted tunnelling regime (high bias voltage and photon energy), electron tunnelling is described by the Fowler–Nordheim (FN) formalism. For electrons tunnelling through a triangular barrier in the presence of a high electric field, the current–voltage characteristics take the form³⁸:

$$I(V_b) \propto V_b^2 \exp\left[-\frac{\beta}{V_b}\right] \quad (1)$$

$$\text{where } \beta = \frac{4d\sqrt{2m}(\Delta - \hbar\omega/2)^{3/2}}{3e\hbar} \quad (2)$$

Here m is the carrier effective mass in the barrier region, and the width d is determined by the BN thickness (see Supplementary Information).

The FN model exhibits several features that serve as fingerprints of a non-thermal carrier tunnelling process, and can be compared directly with experiment. Equation (1) suggests a linear relationship between $\ln(I/V_b^2)$ and $1/V_b$, with a bias-independent slope $-\beta$. To examine the regime over which this behaviour holds, we analysed the $I-V_b$ data taken under supercontinuum laser excitation. Figure 4a shows $\ln(I/V_b^2)$ versus $1/V_b$ at positive bias over a range of photon energies. At high bias or photon energy (Region B in Fig. 2c),

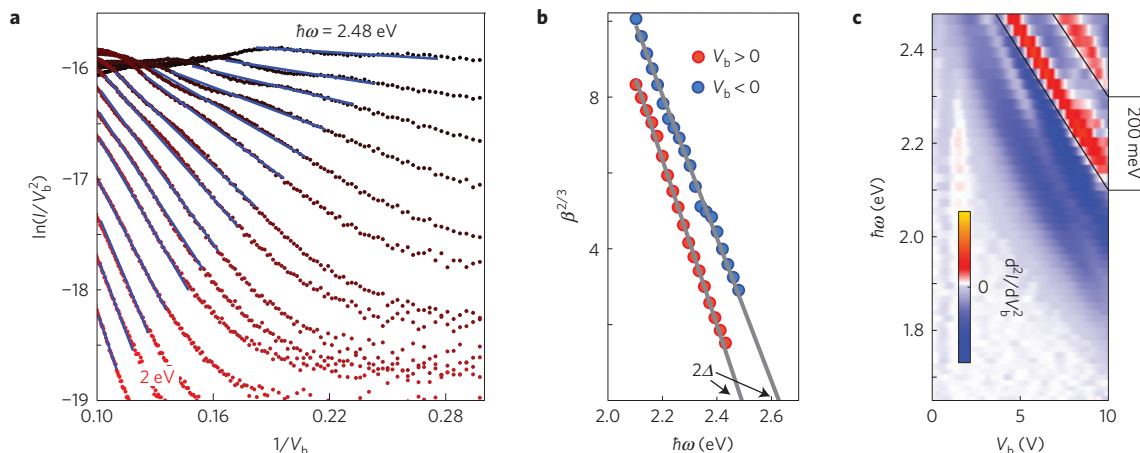


Figure 4 | Experimental signatures of direct Fowler-Nordheim carrier tunnelling. **a**, $\ln(I/V_b^2)$ as a function of $1/V_b$ at different excitation photon energies in the range $\hbar\omega = 2\text{--}2.48$ eV. The blue lines highlight the linear behaviour at high bias, with a slope of $-\beta$. **b**, $\beta^{2/3}$ as a function of $\hbar\omega$ at positive bias (red dots) and negative bias (blue dots). The lines are linear fits with x -intercepts at 2Δ , where $\Delta = 1.25$ and 1.31 eV correspond to the barrier height in the Fowler-Nordheim formula (equation (2) in the text). **c**, d^2I/dV_b^2 map as a function of V_b and $\hbar\omega$. The black lines highlight two oscillation features with a separation of 200 meV. All measurements were carried out with a supercontinuum laser at $T = 100$ K.

we observed a linear relationship that breaks down at low $V_b/\hbar\omega$, where thermionic emission dominates (Region A). We extracted the slope ($-\beta$) from the linear fits, and found that $\beta^{2/3}$ scales linearly with the excitation photon energy $\hbar\omega$, consistent with equation (2) (red dots in Fig. 4b). From fitting the data and comparing to equation (2), we estimate the barrier height from the x -axis intercept to be $\Delta = 1.25$ eV. Similar results were obtained at negative bias (see Supplementary Information), with a slightly higher estimated barrier height $\Delta = 1.31$ eV (blue dots in Fig. 4b). These values agree well with the predicted potential barrier (~ 1.3 eV) between graphene and BN by first-principles calculations³³, and confirm that the photocurrent is dominated by direct carrier tunnelling at high $V_b/\hbar\omega$.

By adjusting the interlayer bias voltage and excitation photon energy, we can tune the interlayer transport process, thus allowing us to pinpoint the regime in which both processes occur on similar timescales. For direct carrier tunnelling, the average lifetime of photoexcited carriers τ_{tun} can be estimated as $\tau_{\text{tun}} = \tau/T(E) \sim h/\Delta E T(E)$, where $\tau \sim h/\Delta E$ is approximated from the uncertainty principle (see Supplementary Information), h is Planck's constant, ΔE is the energy difference between initial and final states, and $T(E)$ is the Wentzel-Kramers-Brillouin (WKB) transmission probability^{38,39}. Both $T(E)$ and τ depend on the excitation energy and bias voltage, whereas $T(E)$ also contains information about the barrier height and effective mass in BN (see Supplementary Information). As a function of bias voltage and photon energy, this model predicts that the average lifetime remains constant over a series of lines in $\hbar\omega$ versus V_b space. Figure 2b shows several of these lines (black dashed lines) and the corresponding times ($\tau_{\text{tun}} = 2, 7, 100$ and $1,000$ fs). Carrier tunnelling occurs faster at high $V_b/\hbar\omega$ than at low $V_b/\hbar\omega$, with τ_{tun} ranging from 1 fs to almost infinity (near zero bias voltage). Our estimate of τ_{tun} exhibits remarkable agreement with experiment. In particular, the contour at $\tau_{\text{tun}} = 7$ fs effectively captures the main transition (blue to red) between features in our photocurrent image. Furthermore, the fit implies a carrier thermalization time of the order of 10 fs in graphene, which indeed matches excellently the results from other ultrafast experiments²³.

In the regime for which the thermalization time matches the carrier lifetime of tunnelling (white-red areas in Fig. 2b), we also observed peculiar behaviours in the I - V_b characteristics, indicating a strong transition between direct tunnelling and thermionic emission. Particularly, we observed an abrupt change of

linearity between $\ln(I/V_b^2)$ and $1/V_b$ (Fig. 4a), which signifies the breakdown of the FN approximation as $V_b/\hbar\omega$ decreases, and hence a diminishing contribution from non-thermal carrier tunnelling. Intriguingly, at the onset of FN tunnelling, weak oscillations in the $\ln(I/V_b^2)$ versus $1/V_b$ plot can be seen. These can be more easily observed by plotting d^2I/dV_b^2 , which changes between negative and positive values as $V_b/\hbar\omega$ increases (blue and red stripes in Fig. 4c). We also observe an additional replica oscillation feature that appears parallel to, yet ~ 200 meV above, the major oscillation feature in the d^2I/dV_b^2 map. These subtle features may indicate resonance effects in the FN tunnelling regime, whose origin could be related to field emission resonances⁴⁰ due to spatial confinement or resonant phonon emission^{38,41,42}. More work, beyond the scope of this manuscript, will be needed to investigate in depth the origin of these resonances.

Methods

Methods and any associated references are available in the [online version of the paper](#).

Received 1 September 2015; accepted 24 November 2015; published online 18 January 2016

References

- Schaller, R. D. & Klimov, V. I. High efficiency carrier multiplication in PbSe nanocrystals: implications for solar energy conversion. *Phys. Rev. Lett.* **92**, 186601 (2004).
- Gabor, N. M., Zhong, Z., Bosnick, K., Park, J. & McEuen, P. L. Extremely efficient multiple electron-hole pair generation in carbon nanotube photodiodes. *Science* **325**, 1367–1371 (2009).
- Lui, C. H., Mak, K. F., Shan, J. & Heinz, T. F. Ultrafast photoluminescence from graphene. *Phys. Rev. Lett.* **105**, 127404 (2010).
- Kim, Y. D. *et al.* Bright visible light emission from graphene. *Nature Nanotech.* **10**, 676–681 (2015).
- Wang, Y. *et al.* Measurement of intrinsic Dirac fermion cooling on the surface of the topological insulator Bi_2Se_3 , using time-resolved and angle-resolved photoemission spectroscopy. *Phys. Rev. Lett.* **109**, 127401 (2012).
- Breusing, M., Ropers, C. & Elsaesser, T. Ultrafast carrier dynamics in graphite. *Phys. Rev. Lett.* **102**, 086809 (2009).
- George, P. A. *et al.* Ultrafast optical-pump terahertz-probe spectroscopy of the carrier relaxation and recombination dynamics in epitaxial graphene. *Nano Lett.* **8**, 4248–4251 (2008).
- Johannsen, J. C. *et al.* Direct view of hot carrier dynamics in graphene. *Phys. Rev. Lett.* **111**, 027403 (2013).
- Gierz, I. *et al.* Snapshots of non-equilibrium Dirac carrier distributions in graphene. *Nature Mater.* **12**, 1119–1124 (2013).

10. Dawlaty, J. M., Shivaraman, S., Chandrashekar, M., Rana, F. & Spencer, M. G. Measurement of ultrafast carrier dynamics in epitaxial graphene. *Appl. Phys. Lett.* **92**, 042116 (2008).
11. Li, T. *et al.* Femtosecond population inversion and stimulated emission of dense Dirac fermions in graphene. *Phys. Rev. Lett.* **108**, 167401 (2012).
12. Ryzhii, V. *et al.* Terahertz photomixing using plasma resonances in double-graphene layer structures. *J. Appl. Phys.* **113**, 174506 (2013).
13. Satou, A., Otsuji, T. & Ryzhii, V. Theoretical study of population inversion in graphene under pulse excitation. *Jpn. J. Appl. Phys.* **50**, 070116 (2011).
14. Boubanga-Tombet, S. *et al.* Ultrafast carrier dynamics and terahertz emission in optically pumped graphene at room temperature. *Phys. Rev. B* **85**, 035443 (2012).
15. Britnell, L. *et al.* Field-effect tunneling transistor based on vertical graphene heterostructures. *Science* **335**, 947–950 (2012).
16. Britnell, L. *et al.* Electron tunneling through ultrathin boron nitride crystalline barriers. *Nano Lett.* **12**, 1707–1710 (2012).
17. Mishchenko, A. *et al.* Twist-controlled resonant tunnelling in graphene/boron nitride/graphene heterostructures. *Nature Nanotech.* **9**, 808–813 (2014).
18. Kittel, C., McEuen, P. & McEuen, P. *Introduction to Solid State Physics* Vol. 8 (Wiley, 1976).
19. Lisowski, M. *et al.* Ultra-fast dynamics of electron thermalization, cooling and transport effects in Ru (001). *Appl. Phys. A* **78**, 165–176 (2004).
20. Fann, W., Storz, R., Tom, H. & Bokor, J. Electron thermalization in gold. *Phys. Rev. B* **46**, 13592–13595 (1992).
21. Neto, A. C., Guinea, F., Peres, N., Novoselov, K. S. & Geim, A. K. The electronic properties of graphene. *Rev. Mod. Phys.* **81**, 109–162 (2009).
22. Tielrooij, K. *et al.* Photoexcitation cascade and multiple hot-carrier generation in graphene. *Nature Phys.* **9**, 248–252 (2013).
23. Brida, D. *et al.* Ultrafast collinear scattering and carrier multiplication in graphene. *Nature Commun.* **4**, 1987 (2013).
24. Song, J. C., Tielrooij, K. J., Koppens, F. H. & Levitov, L. S. Photoexcited carrier dynamics and impact-excitation cascade in graphene. *Phys. Rev. B* **87**, 155429 (2013).
25. Tielrooij, K.-J. *et al.* Generation of photovoltage in graphene on a femtosecond timescale through efficient carrier heating. *Nature Nanotech.* **10**, 437–443 (2015).
26. Gabor, N. M. *et al.* Hot carrier–assisted intrinsic photoresponse in graphene. *Science* **334**, 648–652 (2011).
27. Ma, Q. *et al.* Competing channels for hot-electron cooling in graphene. *Phys. Rev. Lett.* **112**, 247401 (2014).
28. Song, J. C., Reizer, M. Y. & Levitov, L. S. Disorder-assisted electron–phonon scattering and cooling pathways in graphene. *Phys. Rev. Lett.* **109**, 106602 (2012).
29. Graham, M. W., Shi, S.-F., Ralph, D. C., Park, J. & McEuen, P. L. Photocurrent measurements of supercollision cooling in graphene. *Nature Phys.* **9**, 103–108 (2013).
30. Geim, A. & Grigorieva, I. Van der Waals heterostructures. *Nature* **499**, 419–425 (2013).
31. Hong, X. *et al.* Ultrafast charge transfer in atomically thin MoS₂/WS₂ heterostructures. *Nature Nanotech.* **9**, 682–686 (2014).
32. Dean, C. *et al.* Boron nitride substrates for high-quality graphene electronics. *Nature Nanotech.* **5**, 722–726 (2010).
33. Khariche, N. & Nayak, S. K. Quasiparticle band gap engineering of graphene and graphene on hexagonal boron nitride substrate. *Nano Lett.* **11**, 5274–5278 (2011).
34. Rodriguez-Nieva, J. F., Dresselhaus, M. S. & Levitov, L. S. Thermionic emission and negative dI/dV in photoactive graphene heterostructures. *Nano Lett.* **15**, 1451–1456 (2015).
35. Rodriguez-Nieva, J. F., Dresselhaus, M. S. & Song, J. C. Hot-carrier convection in graphene Schottky junctions Preprint at <http://arXiv.org/abs/1504.07210> (2015).
36. Schwede, J. W. *et al.* Photon-enhanced thermionic emission for solar concentrator systems. *Nature Mater.* **9**, 762–767 (2010).
37. Sun, D. *et al.* Ultrafast hot-carrier-dominated photocurrent in graphene. *Nature Nanotech.* **7**, 114–118 (2012).
38. Wolf, E. L. *Principles of Electron Tunneling Spectroscopy* (Oxford Univ. Press, 2011).
39. Sakurai, J. J. & Napolitano, J. *Modern Quantum Mechanics* (Addison-Wesley, 2011).
40. Petersson, G. P., Svensson, C. M. & Maserjian, J. Resonance effects observed at the onset of Fowler–Nordheim tunneling in thin MOS structures. *Solid-State Electron.* **18**, 449–451 (1975).
41. Dai, S. *et al.* Tunable phonon polaritons in atomically thin van der Waals crystals of boron nitride. *Science* **343**, 1125–1129 (2014).
42. Ferrari, A. C. Raman spectroscopy of graphene and graphite: disorder, electron–phonon coupling, doping and nonadiabatic effects. *Solid State Commun.* **143**, 47–57 (2007).

Acknowledgements

We thank V. Fatemi, L. Ju, L. Levitov, J. Rodriguez-Nieva, J. Sanchez-Yamagishi, E. J. Sie, J. C. W. Song and H. Steinberg for discussions. This work was supported by AFOSR Grant No. FA9550-11-1-0225 (measurement and data analysis, Q.M., T.I.A., N.L.N., N.G. and P.J.-H.) and the Packard Fellowship Program. This work made use of the Materials Research Science and Engineering Center Shared Experimental Facilities supported by the National Science Foundation (NSF) (Grant No. DMR-0819762) and of Harvard's Center for Nanoscale Systems, supported by the NSF (Grant No. ECS-0335765). N.G. and C.H.L. have been supported by the Gordon and Betty Moore Foundation's EPiQS Initiative through Grant GBMF4540 for the time-domain photocurrent measurements. F.H.L.K. acknowledges support by Fundacio Cellex Barcelona, the ERC career integration grant (294056, GRANOP), the ERC starting grant (307806, CarbonLight), the Government of Catalonia through the SGR grant (2014-SGR-1535), the Mineco grants Ramón y Cajal (RYC-2012-12281) and Plan Nacional (FIS2013-47161-P), and support by the EC under the Graphene Flagship (contract no. CNECT-ICT-604391). W.F. and J.K. acknowledge the funding support by the STC Center for Integrated Quantum Materials, NSF Grant No. DMR-1231319.

Author contributions

N.M.G. and P.J.-H. conceived the experiment; Q.M., N.L.N. and M.M. fabricated the devices; N.L.N., N.M.G., Q.M. and M.M. carried out the spatial and spectral photocurrent measurements; T.I.A. and C.H.L. performed the time-domain photocurrent measurements under the supervision of N.G.; Q.M., T.I.A., N.L.N. and M.M. analysed the data under the supervision of N.M.G., C.H.L., A.F.Y., F.H.L.K. and P.J.-H.; W.F. and J.K. grew the CVD graphene; K.W. and T.T. synthesized the BN crystals; Q.M., T.I.A., C.H.L., N.L.N., N.M.G., F.H.L.K. and P.J.-H. co-wrote the paper with input from all other authors.

Additional information

Supplementary information is available in the online version of the paper. Reprints and permissions information is available online at www.nature.com/reprints. Correspondence and requests for materials should be addressed to N.M.G. or P.J.-H.

Competing financial interests

The authors declare no competing financial interests.

Methods

Device fabrication. We fabricated G–BN–G heterostructure devices on Si/SiO₂ substrates. The graphene layers were prepared either by mechanical exfoliation of graphite or by chemical vapour deposition (CVD) on a copper surface. In the heterostructure, the bottom layer was either exfoliated graphene, or transferred CVD graphene that was patterned into strips by e-beam lithography and O₂ plasma etching. The middle BN flake was exfoliated from high-quality bulk crystals onto methyl methacrylate (MMA) polymer and transferred onto the bottom graphene. The top graphene layer was similarly exfoliated onto MMA polymer and transferred onto the BN. Finally, we deposited 0.8/80-nm Cr/Au electrodes with e-beam lithography and thermal evaporation.

Photocurrent measurements. We carried out the photocurrent experiment in a confocal microscope. The devices are mounted in an optical cryostat cooled by liquid helium, with controllable temperature in the range of 4–300 K. The excitation beam comes from a broadband supercontinuum fibre laser (Fianium and SuperK). The beam, with wavelength tunable by means of a monochromator, is focused onto the samples with a spot diameter of $\sim 1 \mu\text{m}$. By using a

piezoelectrically controlled mirror, we can scan the beam across the whole device area to obtain photocurrent images. The current is measured by using a lock-in preamplifier at an optical chopper frequency of 77 or 740 Hz.

Two-pulse correlation measurements. We have carried out time-domain photocurrent measurements with an 80-MHz Ti:sapphire oscillator (Tsunami) that generates femtosecond laser pulses with central wavelength 800 nm. The laser is separated into two equally intense beams with controllable path-length difference, and focused onto the devices with a spot diameter of $\sim 2 \mu\text{m}$. Photocurrent was measured as a function of temporal separation between the two pulses. To suppress the interference at zero time delay, the polarizations of the two beams were set to be orthogonal to each other by a half-wave plate. A set of neutral density filters was used to adjust the pump fluence. We have characterized the pulse duration with second harmonic autocorrelation. From the autocorrelation width (~ 130 fs), we determined a pulse duration of ~ 90 fs at our sample position. The response time of the devices is extracted by fitting the photocurrent correlation data with a symmetric biexponential function convolved with a Gaussian function of width ~ 130 fs.